

Effects of orbital drift on land surface temperature measured by AVHRR thermal sensors

Arthur C.R. Gleason, Stephen D. Prince*, Scott J. Goetz, Jennifer Small

Department of Geography, University of Maryland, College Park, MD 20742-8225, USA

Received 21 July 2000; received in revised form 15 January 2001; accepted 15 March 2001

Abstract

The NOAA series of meteorological satellites that carry the Advanced Very High Resolution Radiometer (AVHRR) suffer from orbital drift so that during each satellite's duty period the overpass time occurs later in the day. Replacement satellites restore the overpass time temporarily, but then it gradually decays. The goals of this paper are to document the effects of variable observation time owing to orbital drift on brightness temperatures (BT) and land surface temperature (LST) calculated from them in the NOAA/NASA Pathfinder AVHRR Land (PAL) data set and to consider possible corrections for the resulting trends and discontinuities in the PAL BT data. The drift effects were found to be greater for bare ground than for vegetated land cover classes, however significant effects were found for most vegetated classes. The magnitude of the orbital drift effect for most global cover types was at least as large as the other errors that affect LST measurement. A simple empirical correction for observation time based on solar zenith angle (SZA) was used to correct the PAL BT time series following Gutman [Int. J. Remote Sens. 20 (1999a) 3407]. The correction from this method was compared with that predicted by a physically based model and was found to differ in the early part of each satellite's duty cycle. Finally, the impacts of correction on the effective observation time were analyzed and the simple statistical correction was found to suffer from greater variability than has hitherto been recognized. A modification to the statistical correction to adjust the effective observation time is described. © 2002 Elsevier Science Inc. All rights reserved.

1. Introduction

The Advanced Very High Resolution Radiometer (AVHRR) on the NOAA series of meteorological satellites has, since 1981, provided data that have revolutionized studies of the global land surface. The AVHRR global area coverage (GAC) data set provides global observations over a long time period at regular intervals and relatively high spatial resolution. The length and continuity of this data set lend themselves to the study of land surface interannual and decadal variability and assure that the AVHRR data set will remain valuable even as more technically advanced sensors are developed.

Most uses of AVHRR data for land surface studies have exploited the visible and near-infrared channels to create vegetation indices, principally the normalized difference

vegetation index (NDVI), for monitoring vegetation presence, function and phenology. The AVHRR thermal bands, on the other hand, have been used to a much lesser degree for quantitative studies of the land surface. Three main reasons for this are the difficulty of converting from brightness temperature (BT) to land surface temperature (LST), the indirect relationship of LST with more traditional measures used in energy and water balance studies (e.g., air temperature), and the need for LST data even in the presence of clouds. It should be noted that less quantitatively demanding applications of thermal imagery, such as mapping the aerial extent of fires (Kaufman & Justice, 1998) and snow/ice cover (Hall, Tait, Riggs, & Salomonson, 1998), have not suffered from these limitations to the same degree as energy and water balance applications. This paper is concerned with the observation time of AVHRR measurements, one of the factors related to the accuracy of satellite-derived LST that has received relatively little attention.

A review by Prata (1994) suggests the limiting accuracy of AVHRR-retrieved LST is ± 1.5 K, although controversy persists whether this accuracy is routinely possible over land

* Corresponding author. Tel.: +1-301-405-4062; fax: +1-301-314-9299.
E-mail address: sp43@umail.umd.edu (S.D. Prince).

(Prata, 1998; Prince, Goetz, Dubayah, Czajkowski, & Thawley, 1998). This has led to an accuracy specification of 1 K for the LST product derived from the MODIS instrument (Wan & Snyder, 1996). In practice, achieving such accuracy over the land surface with the AVHRR instrument has proved difficult. Yet, many users' accuracy requirements for LST are quite stringent. For example, Brutsaert, Hsu, & Schmugge (1993) showed that a 0.5 K error in LST can result in a 10% error in sensible heat flux, and Moran & Jackson (1991) estimated a 1 K error in LST would translate to a 10% error in evapotranspiration.

Other uses for LST, for example, biogeochemical modeling, have less demanding requirements for absolute accuracy of LST. However such models can be quite sensitive to trends in LST. Goetz, Prince, Gleason, & Small (2000) used the Global Production Efficiency Model (GLO-PEM, Prince & Goward, 1995) to investigate inter-annual variability of global net primary production (NPP). They found that, for each degree increase in global mean air temperature, global NPP increased by $33 \text{ g Cm}^{-2} \text{ year}^{-1}$ or about 7% of the total. This figure varied greatly by biome, from approximately +5% for boreal and temperate forests to -10% for tropical forests and -100% or more for arid and semiarid regions.

Generating accurate time series of LST involves, first, very accurate sensor characterizations (Czajkowski, Goward, & Ouaidrari, 1998) and calibrations (Weinreb, Hamilton, & Brown, 1990); second, appropriate atmospheric correction algorithms (Prata, 1994; Qin & Karnieli, 1999); finally, and currently most problematic, accurate, representative values for land surface emissivity (Snyder, Wan, Zhang, & Feng, 1998; Wan & Snyder, 1996). These are the main factors affecting the accuracy of AVHRR-derived LST measurements at a single place and time, for example, to compare with concurrent in situ observations. Observation time, however, is another important consideration for the spatial and temporal consistency of LST data sets. If a single site is viewed progressively later in the afternoon over time, it will generally appear to be "cooling" due only to the observation time. Likewise, two sites can be observed on the same day but at different times during the day, presenting a problem for applications that assume instantaneous LST.

Observation time has a number of components. Price (1991) first called particular attention to the impact of drifting overpass time of the NOAA series of satellites (Fig. 1) on measurements of the land surface and suggested orbital modifications that would result in more stable overpass times. The wide scan angle of the AVHRR means that the local time for pixels at the east and west edges of a swath can vary by more than an hour. Furthermore, because the NOAA satellites do not complete an integral number of orbits in a day, the same pixel will be imaged at local times varying up to ± 51 min on successive days, a phenomenon called phasing (McGregor & Gorman, 1994). Finally, the multiscene compositing techniques used to create cloud-free

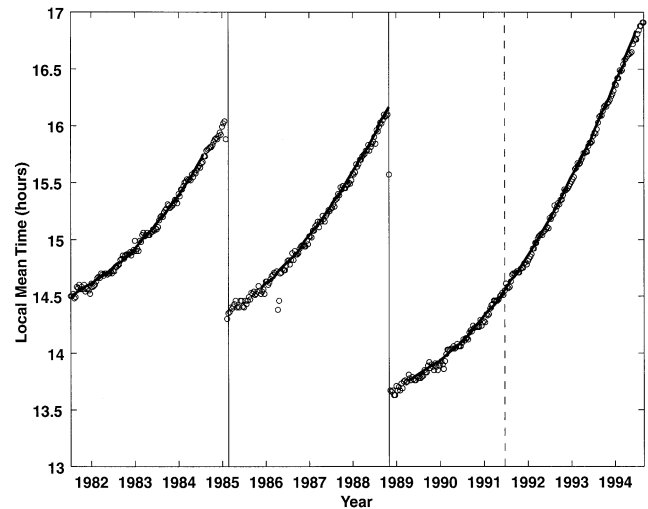


Fig. 1. Equatorial crossing time for NOAA-7, NOAA-9, and NOAA-11. Solid lines are based on antenna-pointing ephemeris computed by propagating NORAD two-line orbital elements for each satellite using SatTrak software, version 3.1 (Bester Tracking Systems, Emeryville, CA). Individual points are the mean t_m for each decade computed using Eqs. (12)–(15) for all pixels within ± 1 degree of the equator and scan angles within 0.2 rad of nadir. Solid vertical lines mark transitions between satellites, and the dashed vertical line marks the eruption of Mt. Pinatubo.

AVHRR data sets mean that neighboring pixels can come from different days and at times differing by up to 2 h (Prince & Goward, 1996). The observation time of a given pixel is therefore a function of observation geometry and compositing as well as long-term orbital drift. Although this paper considers the long-term orbital drift specifically, the results should be applicable to these other aspects of observation time in general.

Relatively few efforts have been made to quantify the effect of orbital drift on AVHRR-derived LST. Gutman (1994), using the second-generation NOAA Global Vegetation Index (GVI) data set (Kidwell, 1997a), observed a 4 K cooling during the lifetime of NOAA-9 for a Middle Eastern desert target. He suggested that the effect of drifting overpass time should be largest in areas where temperature changes quickly over the afternoon, for example, over deserts. Using the newer, third generation GVI data set (Gutman, Tarpley, Ignatov, & Olson, 1995; Kidwell, 1997a), Gutman (1999a) observed approximately 4 and 6 K cooling over the life times of NOAA-9 and NOAA-11, respectively, for a test site in Niger. Traore, Royer, & Goita (1997), also using the GVI, found no trends in LST over study areas in the boreal forest of eastern Canada.

Section 2 of this paper surveys the effects of AVHRR orbital drift in the NOAA/NASA Pathfinder AVHRR Land (PAL) global 8-km data set (Agbu & James, 1994; James & Kalluri, 1994; Smith, Kalluri, Prince, & DeFries, 1997), using more detailed land cover types than have been previously investigated. Documentation of any discontinuities in the PAL thermal data set is important for at least three reasons. First, the PAL data set extends

back to June 1981 while the consistent GVI data set extends back only to April 1985 (earlier GVI data were processed differently) (Kidwell, 1997a). Second, since the PAL data are intended to support climate change research, any potential biases in the time series could affect important conclusions (Goetz et al., 2000). Third, even though the PAL and GVI data sets are derived from the same original GAC data, the processing differs in many ways between these two data sets, including spatial resolution, radiometric resolution, navigation, daily bin method, compositing method, and quality control flagging (Agbu & James, 1994; Gutman et al., 1995; Kidwell, 1997a). The higher order GVI products used in Gutman (1999a) have also been subject to a cloud mask, temporal averaging, and spatial interpolation and smoothing, none of which are used in the PAL data set.

Section 3 of this paper tests an empirical statistical correction for the drift effect. Gutman (1999a) clustered the GVI into six land cover types and demonstrated that monthly BT anomalies were negatively correlated with solar zenith angle (SZA) for every class, although the effect for forested classes was generally less than that for deserts. Gutman then used the regressions from desert and rainforest BT anomaly with SZA anomaly to correct for the drift effect. Obvious effects of drifting overpass time for a 2.5 square degree area in the Sahel were removed. We apply this method to the PAL data set, assess its ability to remove obvious drift effects in this newer data set, and propose a modification designed to correct all pixels to a standard observation time.

2. Survey of orbital drift effects in the PAL data set

The goal of this section is to determine for which land cover types the changes in observation time associated with sensor changes noticeably affect the time series of PAL BT. To do this, detailed land cover types are considered and a ranking scheme is developed to define “noticeable impact.”

2.1. Data

The PAL 10-day, 8-km global data set for the time period June 1981 to September 1994 was acquired from the NASA Goddard Space Flight Center Distributed Active Archive Center (DAAC) along with the ancillary latitude, longitude, and land mask files. Channels 1, 4, 5, and the scan and SZA were extracted from the 12 layers available for each 10-day period (decade). The Hansen, DeFries, Townshend, & Solberg (2000) land cover map used in this study identifies 13 land surface classes (Table 1) and is available on an equal-angle latitude longitude grid at 0.00833° spatial resolution (approximately 1 km at the equator). For comparison with the PAL data, this map was aggregated to 0.0625° spatial resolution then projected to

Table 1

Land cover classes from Hansen et al. (2000) presented in the four groups that were used for aggregating from 1 to 8 km spatial resolution

| Class name | Number |
|------------------------------------|--------|
| <i>Forest and woodland classes</i> | |
| Evergreen needleleaf | 1 |
| Evergreen broadleaf | 2 |
| Deciduous needleleaf | 3 |
| Deciduous broadleaf | 4 |
| Mixed forest | 5 |
| Woodland | 6 |
| Wooded grassland | 7 |
| <i>Shrubland classes</i> | |
| Closed shrubland | 8 |
| Open shrubland | 9 |
| <i>Grass and crop classes</i> | |
| Grassland | 10 |
| Crops | 11 |
| <i>Nonvegetated classes</i> | |
| Bare | 12 |
| Urban | 13 |

Results for the deciduous needleleaf and urban classes (#3 and #13) are not presented (see text for discussion).

the Goode Interrupted Homolosine grid at 8-km resolution. Because a simple majority filter tends to underrepresent the forest classes, the aggregation was performed using a two-step process. First, each of the 13 original cover types was assigned to one of four broad groups (Table 1): forest and woodland (Classes 1–7), shrubland (Classes 8 and 9), grasses/crops (Classes 10 and 11), or nonvegetated (Classes 12–13). Then, each 0.0625° coarse pixel was assigned to the broad cover type that represented the majority of 0.00833° fine pixels falling within it. Finally, the original cover type with the highest frequency in the assigned broad class was selected as the class for the aggregated pixel. PCI software (PCI, Ontario, Canada) was used to project the aggregated 0.0625° data to the PAL Goode Interrupted Homolosine grid.

The urban class (#13) was omitted from all analysis because of its extremely small sample size (0.18% of global area). The deciduous needleleaf class (#3) was also omitted because the preprocessing steps described in this section discarded all the pixels in this class for several decades each winter. Thus, we considered 11 distinct land cover classes.

2.2. Preprocessing

First, all ocean pixels defined by the PAL land mask were excluded. Second, any missing Channel 4 or 5 pixels were removed; the vast majority of these were located in high latitudes during winter. Third, Channels 4 and 5 values outside the range 160–320 K were discarded as below or above the range of the instrument (Agbu & James, 1994; Prince & Goward, 1996). Fourth, three simple tests for

clouds were used following Prince & Goward (1995). Pixels were discarded that had either Channel 1 reflectance >20%, Channel 4 or 5 BT (T4, T5) <253 K, or a T4–T5 difference greater than a prescribed threshold (Eq. (1)).

$$\text{For T4} = \begin{cases} < 260 \\ 260 - 305 \\ > 305 \end{cases}$$

$$(T4 - T5)_{\max} = \begin{cases} 0 \\ -13443 + 194.9(T4) - 1.0563(T4)^2 \\ + 0.002534(T4)^3 - 0.000002268(T4)^4 \\ 7.8 \end{cases} \quad (1)$$

The 20% reflectance filter was not used for the bare class, because it caused almost every bare pixel to be discarded. A 20% threshold may remove snow pixels, except where overlying forest canopy reduces the resulting reflectance to <20%. This simple cloud masking approach should suffice for the purposes of this paper even though more sophisticated cloud screening algorithms are desirable to exploit the full information content of AVHRR data sets (Gutman, Ignatov, & Olson, 1994). The cloud mask distributed with PAL appears overly conservative (Prince & Goward, 1996), so effectively there is no “standard” cloud mask scheme for PAL and users must develop their own techniques. This differs from the third generation GVI data set used by Gutman (1999a) and Traore et al. (1997), which has cloud flags for weekly products and a preapplied cloud screen and cloud gap fill procedure for monthly products. The most noticeable effect of a more sophisticated cloud-screening algorithm should be to reduce variability in a time series of the data. If anything, this should make the drift effect more apparent, especially in plots of anomaly time series. Finally, because the data transformations described below take averages over very large areas, it is likely that clear sky pixels will greatly outnumber the cloudy pixels that pass through our simple filter. On balance, we felt it was more important to demonstrate these results using a simple filter rather than one so complex others could not easily implement it.

Three decades were missing from the data set: 1981 decade 32, 1983 decade 29, and 1992 decade 15. Mean values for these time periods were interpolated from those of preceding and following decades. As mentioned above, the deciduous needleleaf class (#3) was entirely obscured by clouds or null values for many of the decades considered, including several months each winter, so it was omitted from all of the following analysis.

2.3. Data transformations

T4 and T5 were averaged by land cover class to create a spatial mean value for each time step (see Appendix A for details). Anomaly time series ($\delta T4$, $\delta T5$) for each land cover type were computed by subtracting the appropriate decadal mean over the 14-year time series from each decade (see Appendix A for details). A generalized distance time series (Davis, 1986) was computed for both the original and anomaly series.

The generalized distance D^2 is a boundary-locating algorithm designed to detect sudden changes in mean value over a given segment of length $2h+1$ of the temporal window being considered, where h is a specified number of time steps. D^2 was calculated for every time step j of each time series T ($T=T4$, $T5$) as well as for every time step of each anomaly time series δT ($T=T4$, $T5$) using:

$$D_j^2 = \frac{(\bar{X}_1 - \bar{X}_2)^2}{s_1^2 + s_2^2} \quad (2)$$

Here \bar{X}_1 is the mean of observations over the window from observation X_{j-h} to X_j , \bar{X}_2 is the mean of observations over the window from observation X_j to X_{j+h} , and the denominator is simply the sum of the variances (s^2) computed over each of the two parts of the window around X_j .

A value of $h=35$ decades was chosen. This gives a sliding window of 2 years, which ensured the statistic was not overly sensitive to seasonal fluctuations, but changes in the mean values between consecutive 12-month periods should be identified. It should be noted that the magnitude of D^2 is only relevant within a given time series, and values cannot be compared between different time series. With smooth data, D^2 peaks at any discontinuity, but the addition of noise can broaden, skew, and even shift the period in which D^2 peaks. Thus, the generalized distance should be interpreted with caution and in concert with other statistics.

2.4. Analysis

Identification of “noticeable” discontinuities in a time series is inherently subjective, because such a term may mean different things to different users. We used a ranking scheme (Table 2) for the four time series (T , δT , $D^2(T)$, and $D^2(\delta T)$) to make this process more objective. Each of the four time series for each land cover class was ranked based on the criteria in Table 2, and the four values were averaged to give a single overall rank for the class.

The major advantage of this approach is to standardize what is meant by *obvious* (ranking=1), *noticeable* (ranking=2), and *not significant* (ranking=3) for each of the four time series for each class. An overall class ranking less than or equal to 2 indicates noticeable impact of discontinuities.

Table 2

Criteria and scores for ranking the effects of drift and satellite changes on brightness temperatures (T_4 , T_5), their anomalies (δT_4 , δT_5), and generalized distance of each of these ($D^2(T_4)$, $D^2(T_5)$, $D^2(\delta T_4)$, $D^2(\delta T_5)$)

| Rank | |
|---|--|
| <i>T₄ and T₅</i> | |
| 1 | Discernable cooling trend over lifetime of satellite and temperature jump between satellites. |
| 2 | Discernable difference in mean temperature levels between satellites. |
| 3 | No discernable trends or discontinuities |
| <i>δT_4, δT_5</i> | |
| 1 | Discernable cooling trend over lifetime of satellite and temperature jump between satellites that occur over a single decade. |
| 1.5 | One satellite transition qualifies for a value of 1 and the other qualifies for a value of 2. |
| 2 | Transition from a series of several decades with anomalies less than minus one standard deviation before the satellite shift to several decades with anomalies greater than plus one standard deviation after the shift. |
| 3 | Failure to meet Criterion 1 or 2. Note that all classes have a negative slope of δT versus solar zenith angle, so there is some impact for every class. A value of 3 simply indicates that the relationship is relatively unimportant, not that it is nonexistent. |
| <i>D^2</i> | |
| 1 | Peak in D^2 time series within one decade of satellite shift and peaks associated with satellite shift are two of the three largest peaks in entire time series. |
| 1.5 | Peaks with tails, which overlap satellite shift, are the two largest in the time series, and one of the two peaks is within one decade of a satellite shift. |
| 2 | Peaks with tails, which overlap satellite shift, are among three largest in the time series. |
| 3 | Failure to meet Criterion 1 or 2. |

Such standardization improves our ability not only to assess the impact of orbital drift on each land cover class, but also to assess the success of each correction to the data. Furthermore, the ranking scheme provides a way to evaluate the data without resorting to external data sets, which is useful since no comparable in situ global data on LST exists. Finally, the ranking scheme provides a convenient way to summarize many results.

2.5. Results

Spatial mean time series (T , δT , $D^2(T)$, and $D^2(\delta T)$) were created for each land cover class over three large geographic areas: the entire globe, the Northern, and the Southern Hemisphere. The hemispheres were separated to determine if averaging data from different seasons, as in the global time series, had any impact on the results.

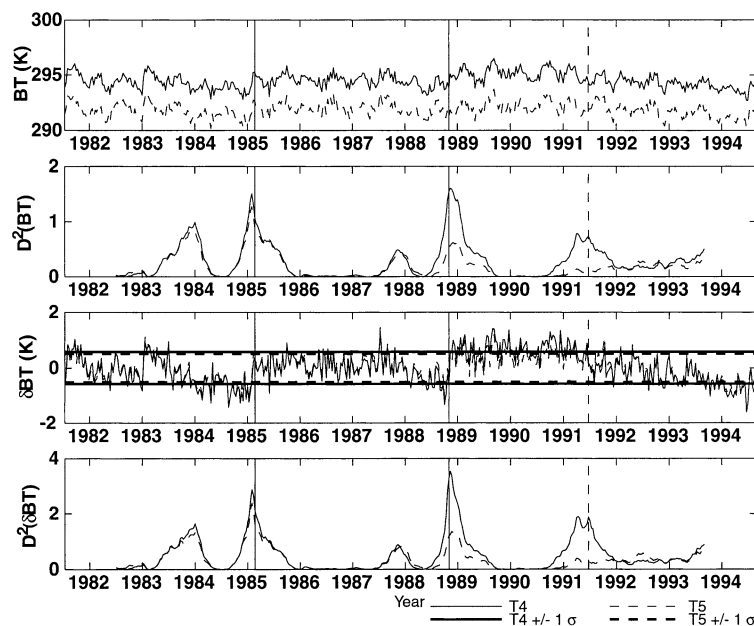


Fig. 2. Spatially averaged uncorrected time series for Class 2, evergreen broadleaf. Top panel: T_4 and T_5 . Second panel: $D^2(T_4)$ and $D^2(T_5)$. Third panel: δT_4 and δT_5 . Bottom panel: $D^2(\delta T_4)$ and $D^2(\delta T_5)$. Satellite transitions are shown as solid vertical lines, and the eruption of Mt. Pinatubo in June 1991 is shown as a dashed vertical line.

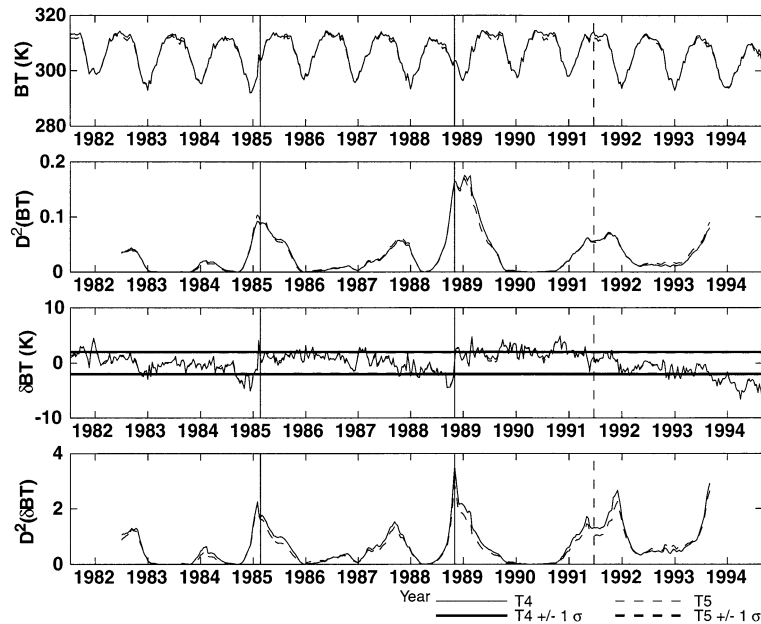


Fig. 3. Spatially averaged uncorrected time series for Class 12, bare ground. Top panel: T4 and T5. Second panel: $D^2(T4)$ and $D^2(T5)$. Third panel: $\delta T4$ and $\delta T5$. Bottom panel: $D^2(\delta T4)$ and $D^2(\delta T5)$. Satellite transitions are shown as solid vertical lines, and the eruption of Mt. Pinatubo in June 1991 is shown as a dashed vertical line.

The Channels 4 and 5 global mean time series for the broadleaf evergreen (#2) and bare (#12) classes are shown in Figs. 2 and 3 to indicate the performance of these four metrics. Global Channel 4 anomaly time series ($\delta T4$) for all land cover classes are shown in Fig. 4. T5 was lower than T4 as expected owing to the greater absorption of the Channel 5 wave band by atmospheric water vapor (Figs. 2a and 3a). Abrupt transitions at satellite replacements (marked with vertical solid lines) were apparent in the anomaly time series (Figs. 2c, 3c, and most of Fig. 4). Cooling trends over the life of both NOAA-7 and NOAA-9 were apparent for the bare class (Fig. 3a,c) and during the NOAA-7 period for the evergreen broadleaf class (Fig. 2a,c). The generalized distance calculations (Figs. 2b,d and 3b,d) also indicated strong peaks coincident with the satellite replacements.

The overall rankings by class (Table 3) indicate that the change in observation time due to drift and satellite replacements affected most classes to a noticeable degree for both T4 and T5. Generally, the effects were less over vegetated classes than over bare classes. However, contrary to previous suggestions that orbital drift does not affect LST over vegetation, our results show that the drift effect was absent or small only for evergreen needleleaf, deciduous broadleaf and mixed forests, which were the only land cover types examined in the Traore et al. (1997) study. In our results, most vegetation types, including the largest forest class (evergreen broadleaf) showed obvious orbital drift effects (Fig. 2 and Table 3). Furthermore, although the drift effect was certainly distinct in the bare class, several other classes appeared to

be at least as sensitive to changes in overpass time, if not more so.

The somewhat lower rankings for Southern Hemisphere classes in Table 3 relative to the global and Northern Hemisphere rankings indicate that satellite changes affect the Southern Hemisphere more strongly than the Northern Hemisphere. This can be seen more clearly by subtracting the mean $\delta T4$ of the last three decades before each satellite switch from the mean of the first three decades after each satellite switch. These differences are larger in the Southern Hemisphere than the Northern Hemisphere for most classes (Table 4). In addition, Table 4 indicates that the magnitude of the NOAA-9 to NOAA-11 discontinuity was larger than that for NOAA-7 to NOAA-9. The same analysis for $\delta T5$, and for means taken over 1 and 36 decade windows, all yielded similar results.

2.6. Impact on LST

The results show that, for large area averages, the time series of PAL T4 and T5 were significantly affected by orbital drift for most land cover classes. The results also reveal that T4 and T5 are not always affected to the same degree; the discontinuities are of different magnitudes, and plots of $\delta T4$ and $\delta T5$ do not always overlap. An important question is whether the (T4–T5) term used in many split window LST formulations automatically compensates for the drift effect. To test this, we performed the identical analysis described above, but used LST computed with two widely used split window formulae; the Sobrino, Coll, &

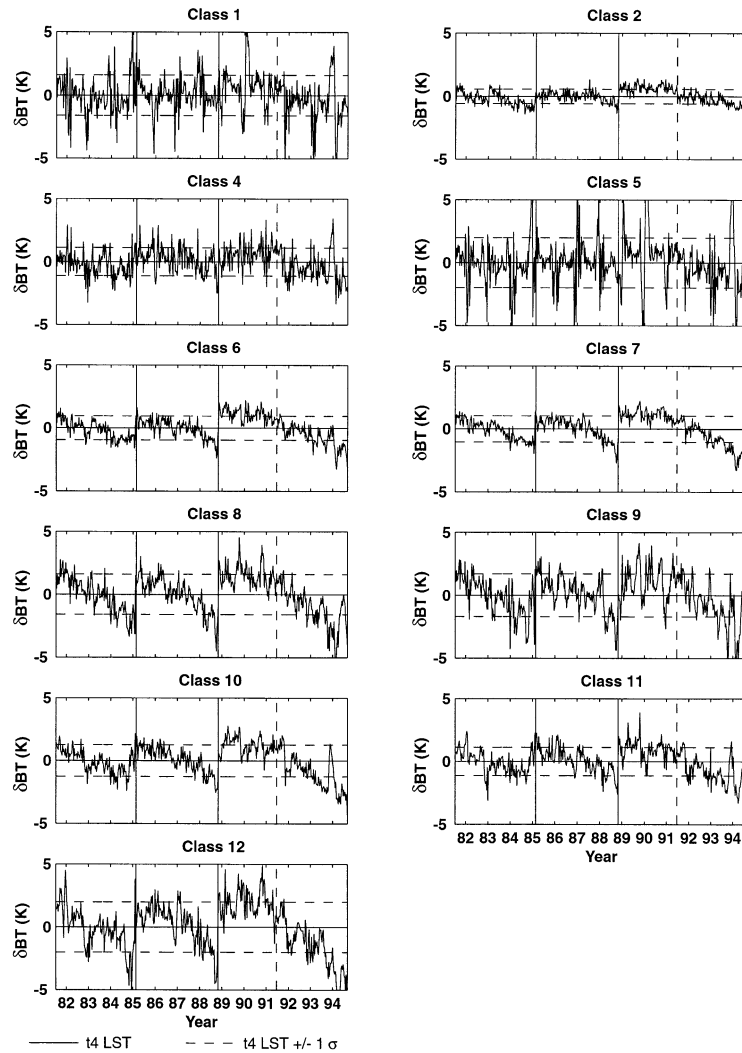


Fig. 4. Anomaly time series (δT_4) for every class. Satellite transitions are shown as solid vertical lines, and the eruption of Mt. Pinatubo in June 1991 is shown as a dashed vertical line.

Caselles (1991) and Ulivieri, Castronuovo, Francioni, & Cardillo (1994) equations, which were chosen because the necessary split window coefficients were available for the entire PAL record.

Ulivieri et al. (1994)

$$LST = A * T_4 + B * (T_4 - T_5) \quad (3)$$

Sobrino et al. (1991)

$$LST = A + B * T_4 + C * (T_4 - T_5) + D * (T_4 - T_5)^2 \quad (4)$$

where T_4 and T_5 are BT in AVHRR Channels 4 and 5, and A , B , C , and D are coefficients computed by Ouaidrari, Goward, Czajkowski, Sobrino, Liang & Vermote (2001) for each satellite (Table 5). The results for the evergreen broadleaf (#2) and bare (#12) classes were virtually identical

for these two algorithms (Fig. 5). Results for the other classes were similar, and indicate that the drift effect observed in T_4 and T_5 was not inherently compensated for by split window algorithms. In fact, for Class 2, the transformation to LST increased the discontinuity between sensors (overall ranking of 1 using either algorithm). Further comparison of the performance of the many LST split-window algorithms is beyond the scope the present paper.

3. Test of a statistical correction

Having identified significant trends and discontinuities in time series of PAL BT, we evaluated the success of Gutman's (1999a) correction for the GVI data set when applied to the PAL data. The technique uses a regression of δBT on

Table 3
Overall rankings of PAL T4 and T5 for each land cover class

| Class | Global | | Northern Hemisphere | | Southern Hemisphere | |
|-------------------------|------------|------------|---------------------|------------|---------------------|------------|
| | T4 | T5 | T4 | T5 | T4 | T5 |
| 1: Evergreen needleleaf | 3.0 | 3.0 | 3.0 | 3.0 | 1.0 | 1.0 |
| 2: Evergreen broadleaf | 1.5 | 1.8 | 1.5 | 1.5 | 2.0 | 2.8 |
| 4: Deciduous broadleaf | 2.5 | 3.0 | 3.0 | 3.0 | 2.5 | 2.5 |
| 5: Mixed forest | 3.0 | 3.0 | 3.0 | 3.0 | 3.0 | 3.0 |
| 6: Woodland | 1.0 | 1.0 | 1.8 | 1.8 | 1.1 | 1.1 |
| 7: Wooded grassland | 1.0 | 1.0 | 1.5 | 1.5 | 1.0 | 1.0 |
| 8: Closed shrubland | 1.0 | 1.0 | 1.0 | 1.0 | 1.0 | 1.0 |
| 9: Open shrubland | 1.8 | 1.8 | 1.5 | 1.5 | 1.0 | 1.0 |
| 10: Grassland | 1.3 | 1.3 | 1.4 | 1.4 | 1.1 | 1.1 |
| 11: Crops | 1.4 | 1.4 | 1.9 | 1.9 | 1.0 | 1.0 |
| 12: Bare | 1.0 | 1.0 | 1.0 | 1.0 | 1.0 | 1.0 |

These are average values for each class of the rankings for each of the four parameters (T , $D^2(T)$, δT , $D^2(\delta T)$), where T is T4 or T5). Classes with noticeable impact (overall ranking ≤ 2) are in bold face.

coincident observations of SZA anomalies ($\delta\theta$). Note that such a correction is based on average conditions over an entire land cover class, and will therefore reconstruct only the long term average temperature change as a function of SZA, not individual events such as passage of an atmospheric front.

After calculating the correction coefficients, they were tested on large samples (global and hemispherical averages) and on local samples (test sites of a few degrees square). The correction for the bare class was also compared with what would be expected based on a modeled climatology of LST. These results are not intended as a validation, since in situ data or remotely sensed data from another source were not available. The point was to determine whether the statistical correction removes noticeable discontinuities as defined in Table 2, not to validate the result in an absolute sense.

Table 4
Three-month averages of δT_4 (K) after each sensor switch minus three-month averages of δT_4 before sensor switch

| Class | Global | | Northern Hemisphere | | Southern Hemisphere | |
|-------------------------|------------|------------|---------------------|------------|---------------------|------------|
| | 7-9 | 9-11 | 7-9 | 9-11 | 7-9 | 9-11 |
| 1: Evergreen needleleaf | 0.2 | 0.9 | 0.5 | 0.7 | 0.7 | 3.5 |
| 2: Evergreen broadleaf | 0.7 | 1.1 | 0.8 | 1.3 | 0.5 | 1.1 |
| 4: Deciduous broadleaf | -0.3 | 1.8 | 0.5 | 2.0 | 0.2 | 2.0 |
| 5: Mixed forest | 1.3 | -0.1 | 2.6 | -0.2 | 0.1 | 3.4 |
| 6: Woodland | 1.4 | 2.9 | 1.9 | 1.9 | 1.1 | 3.8 |
| 7: Wooded grassland | 1.4 | 3.1 | 1.5 | 2.7 | 1.4 | 3.7 |
| 8: Closed shrubland | 2.4 | 4.8 | 1.5 | 5.0 | 3.5 | 4.7 |
| 9: Open shrubland | 2.1 | 3.1 | 1.7 | 3.9 | 3.7 | 4.2 |
| 10: Grassland | 0.8 | 2.5 | 0.8 | 2.6 | 1.2 | 4.5 |
| 11: Crops | 1.1 | 3.5 | 0.7 | 2.8 | 3.1 | 6.4 |
| 12: Bare | 1.0 | 5.9 | 1.2 | 5.9 | 5.0 | 8.6 |

Differences greater than 1 K are in bold face.

Table 5
Coefficients used for computing LST using Eqs. (3) and (4) (from Ouadrari et al., 2001)

| Satellite | Ulivieri Eq. (1) | | Sobrino Eq. (2) | | | |
|-----------|------------------|--------|-----------------|--------|--------|--------|
| | A | B | A | B | C | D |
| NOAA-7 | 0.9960 | 2.8094 | 10.7178 | 0.9627 | 1.6471 | 0.2960 |
| NOAA-9 | 0.9974 | 3.0334 | 5.2568 | 0.9827 | 1.6378 | 0.3677 |
| NOAA-11 | 0.9961 | 2.9484 | 7.5789 | 0.9738 | 1.6199 | 0.3317 |

3.1. Method

Gutman's technique consists of five steps. In the following description, δT (BT anomaly) represents either δT_4 or δT_5 , but also works for δLST .

(1) Stratify the data set into six land cover classes based on annual mean and range of NDVI, and Channel 4 BT (see Gutman, 1999b for details).

(2) Compute the anomaly time series $\delta\theta$ of SZA, which, for a given pixel i and time step j , is the difference between the SZA θ_{ij} and the mean SZA for that pixel and time step over the duration of the data set Z (see Appendix A for definition of indices):

$$\theta_{ij}^{\text{mean}} = \frac{1}{Z} \sum_{\substack{k=j(\text{mod } Y) \\ 1 \leq k \leq J}} \theta_{ik} \quad (5a)$$

$$\delta\theta_{ij} = \theta_{ij} - \theta_{ij}^{\text{mean}} \quad (5b)$$

Transform each $\delta\theta_{ij}$ relative to 45° :

$$\theta'_{ij} = 45 + \delta\theta_{ij} \quad (6)$$

Take the cosine of each θ'_{ij} , and for each time step j take the spatial mean over all pixels i of the values $\cos(\theta'_{ij})$:

$$\cos(\theta')_j = \frac{1}{I} \sum_{i=1}^I \cos(\theta'_{ij}) \quad (7)$$

(3) Compute coefficients a and b using least square regression of δT on $\cos(\theta')$ for land cover classes with minimum and maximum annual NDVI:

$$\delta T_j = a + b(\cos(\theta')_j) \quad (8)$$

(4) Interpolate the regression coefficients to other land cover classes defined in Step 1 (Eqs. (9a) and (9b)):

$$a_L = a_{\min} V_L + a_{\max}(1 - V_L) \quad (9a)$$

$$b_L = b_{\min} V_L + b_{\max}(1 - V_L) \quad (9b)$$

Here a_L and b_L are the coefficients for vegetation class L , a_{\min} and b_{\min} are the coefficients for the class with minimum NDVI, a_{\max} and b_{\max} are the coefficients for the class with maximum NDVI, and $V_L = (N_{\max} - N_L)/(N_{\max} - N_{\min})$,

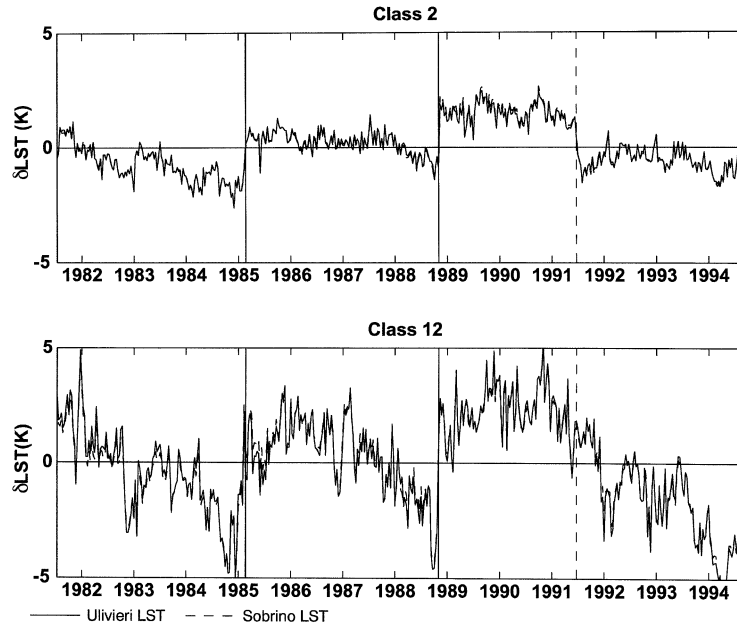


Fig. 5. Evergreen broadleaf (Class 2) and bare (Class 12) anomaly time series for two LST algorithms, which give virtually identical results. Satellite transitions are shown as solid vertical lines, and the eruption of Mt. Pinatubo in June 1991 is shown as a dashed vertical line.

where N is the NDVI. This yields a delta function for each land cover class:

$$\Delta_{L_j} = a_L + b_L \left(\cos(\theta)_j \right) \quad (10)$$

(5) Finally, generate the corrected anomaly time series δT^* by subtracting the delta function for the appropriate land cover class from the original anomaly time series δT at each time step j :

$$\delta T_j^* = \delta T_j - \Delta_j \quad (11)$$

This last step works only when the mean value of Δ_j approximately equals zero. If Δ_j has a nonzero mean, it is necessary to compute $T_j^* = T_j - \Delta_j$ and then the corrected anomalies from T_j^* (see Appendix A).

We applied this method to the PAL BT data, using the Hansen et al. (2000) land cover dataset in place of Step 1. The bare (class #12) and evergreen broadleaf (class #2) classes served as our minimum and maximum NDVI endpoints for regression, respectively. This resulted in the following coefficients for T4: $a_{\min} = -10.94$, $b_{\min} = 15.67$, $a_{\max} = -2.27$, $b_{\max} = 3.27$, and the following coefficients for T5: $a_{\min} = -10.65$, $b_{\min} = 15.25$, $a_{\max} = -1.74$, $b_{\max} = 2.5$. The annual mean NDVI values used in Step 4 for interpolation between Classes 12 (N_{\min} = low NDVI) and 2 (N_{\max} = high NDVI) are given in Table 6.

3.2. Results I: stabilization of large samples

We applied the statistical correction to the global and hemispherical time series for each class and evaluated the results using the criteria from Table 2. This tested the ability of each cover-specific global correction to remove obvious

trends in the population of values from which it was derived and on fairly large samples of that population. Almost every corrected time series received a ranking greater than 2.0, indicating that most obvious discontinuities due to satellite changes were removed. The exceptions were Classes 11 (crops) and 12 (bare) in the Southern Hemisphere, which had postcorrection rankings of 1.4 and 1.0, respectively, for both T4 and T5.

3.3. Results II: stabilization of local samples

We also tested the application of the correction to local samples, since local time series can differ greatly from the aggregate mean. The sites chosen fell into three broad categories: (1) sites similar to those used in previous studies, (2) intermediate vegetation sites (not bare, not fully forested), since these have not been previously investigated, and (3) classes which appeared not to be sufficiently corrected in

Table 6
Annual mean NDVI for each class used to interpolate coefficients for the statistical correction between Classes 2 and 12

| Class name | NDVI |
|-------------------------|------|
| 1: Evergreen needleleaf | 0.43 |
| 2: Evergreen broadleaf | 0.58 |
| 4: Deciduous broadleaf | 0.56 |
| 5: Mixed forest | 0.47 |
| 6: Woodland | 0.44 |
| 7: Wooded grassland | 0.39 |
| 8: Closed shrubland | 0.23 |
| 9: Open shrubland | 0.13 |
| 10: Grassland | 0.28 |
| 11: Crops | 0.39 |
| 12: Bare | 0.05 |

the Southern Hemisphere using global coefficients. The time series for each site was created by averaging over a few square degrees rather than entire land cover class globally or by hemisphere. The same ranking criteria (Table 2) were used to assess the effect of orbital drift before and after applying the global correction (Table 7).

The results for Sites a (Sahara desert) and b (boreal forest) confirmed previous work indicating that a correction of the form proposed by Gutman (1999a) is both necessary and sufficient for low latitude Northern Hemisphere deserts, and that such a correction is not needed for the boreal forest. Also note that the correction for evergreen needleleaf forest was weak enough so that, when applied to the boreal forest site, it did not introduce an artificial, noticeable trend.

Sites c (South Central African woodland) and e (South Central African wooded grassland) suffered from significant drift-induced cooling over areas that were not fully forested. They also indicated that a correction derived from global samples could successfully correct localized time series of BT for these land cover types.

The lack of an obvious drift signal in the raw data for Site d (crops in central USA) was unexpected, since the Northern Hemisphere crop class as a whole did show signs of noticeable cooling (Tables 3 and 4). As with Site b, however, applying the global crop correction to the time series for this site did not introduce artificial discontinuities.

Site f (Namib desert) suffered strong drift-induced cooling, which was consistent with expectations for a bare class, however, the global correction derived for the bare class was not sufficient to remove observed drift effects at this site. A second set of correction coefficients was derived

using Eqs. (8)–(11), but using only the Southern Hemisphere samples for Classes 2 and 12, rather than the global populations in the regression (8). This resulted in a new set of coefficients for T4: $a_{\min} = -17.75$, $b_{\min} = 25.58$, $a_{\max} = -2.15$, $b_{\max} = 3.1$, and the following coefficients for T5: $a_{\min} = -17.02$, $b_{\min} = 24.52$, $a_{\max} = -1.61$, $b_{\max} = 2.33$. These were interpolated to other classes using the NDVI from Table 6, resulting in a Southern Hemisphere correction that was sufficient to remove the discontinuities for Site f (ranking of 3 when corrected in this way).

Sites g (South America crops) and h (Western Australia crops) deviated significantly from other results. Neither the global nor the Southern Hemisphere correction removed the obvious drift-induced discontinuities in these time series. Yet another correction from the local sample itself was needed to generate corrected time series with rankings greater than 2.

Taken together, these results indicate that the global correction worked well in most places, though the bare class required a separate correction for the Southern Hemisphere, and the Southern Hemisphere crop class required a locally specific correction.

3.4. Results III: comparison with modeled climatology

The regression correction discussed in the previous two sections created an empirical climatology of BT or LST change over the afternoon then adjusted each observation by an amount proportional to the difference between the time of the specific observation and the reference time of the climatology. A similar approach can be used with a climatology from any source, for example, from in situ

Table 7

Local sites for testing global corrections and their rankings before and after applying the global correction by land cover type

| Site | Class | Location | Rank before global correction | Rank after global correction |
|--|-------|----------------------------|-------------------------------|------------------------------|
| <i>Test sites similar to previous studies</i> | | | | |
| a: Sahara Desert | 12 | 21.5N–24.5N 12E–15E | 1.5 | 3.0 |
| b: Boreal Forest | 1 | 51N–54N 66W–69W | 3.0 | 3.0 |
| <i>Test sites with moderate levels of vegetation</i> | | | | |
| c: Woodland | 6 | 11S–15S 24E–28E | 2.0 | 2.8 |
| d: USA crops | 11 | 39.5N–41.5N 82.5W–88.5W | 3.0 | 3.0 |
| e: Wooded grassland | 7 | 15.5S–19.5S 17E–21E | 1.5 | 2.5 |
| <i>Test sites for Southern Hemisphere classes not fully corrected with global coefficients</i> | | | | |
| f: Namib Desert | 12 | 22S–25S 13.5E–16.5E | 1.0 | 1.5 |
| g: S. America crops | 11 | 35S–39S 57.5W–64.5W | 1.0 | 1.5 |
| h: W. Australia crops | 11 | 32S–35S 117E–120E | 1.0 | 1.4 |

Rankings ≤ 2.0 , in bold, indicate noticeable impact.

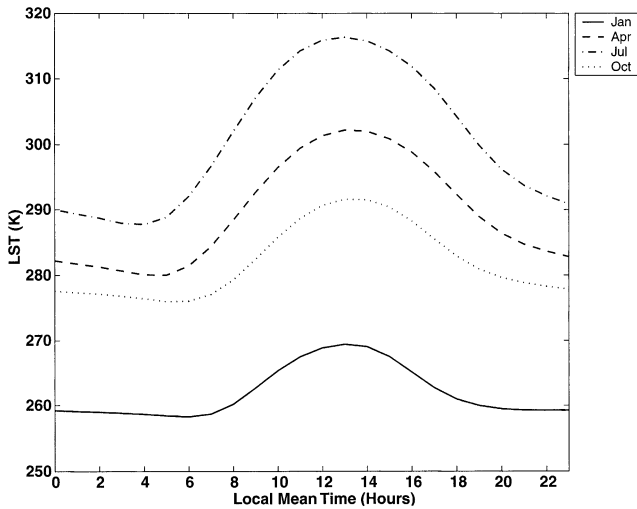


Fig. 6. Climatological diurnal cycles for the bare ground class between 40°N and 45°N developed by Jin & Dickinson (1999). Solid line is for January, dashed line is for April, dash dot line is for July, and dotted line is for October. Other months are not shown for clarity, but have similar shapes.

observations or a physical model. A comparison of the regression correction discussed above with one derived from an independent climatology would indicate whether the magnitude of the regression correction was realistic. Appropriate observations unfortunately are very few as are modeled climatologies. Privette, Fowler, Wick, Bald-

win, & Emery (1995) used a model of sea surface temperature (SST) to analyze the effect of orbital drift on SST retrievals, and Jin & Dickinson (1999) have recently developed an appropriate model for LST that we use here.

The monthly climatological diurnal LST tables from Jin & Dickinson (1999) for the bare ground class (#12) between 40°N and 45°N (Fig. 6), and the time series of mean observation time for those pixels in each decade (Eqs. (12)–(15)) were used to generate a look up table of LST deviations from a 2 p.m. reference time for each decade in the data set. This is analogous to the empirical delta function (11).

Unfortunately, the PAL data set only provides observation time for a given pixel to the nearest hour, however, local observation time can be calculated for a given pixel using Eq. (12) (Goward, Turner, Dye, & Liang, 1994):

$$HA = \arccos \left[\frac{\cos(\theta) - \sin(\lambda)\sin(\delta)}{\cos(\lambda)\cos(\delta)} \right] \text{ (in degrees)} \quad (12)$$

Here, HA is the hour angle of an observation, θ is SZA, λ is latitude, and δ is solar declination, which we estimated using:

$$\delta = 23.45 \sin(360(D_y + 284)/365.25) \text{ (in degrees)} \quad (13)$$

where D_y is the day of year. In this case, we took D_y as the

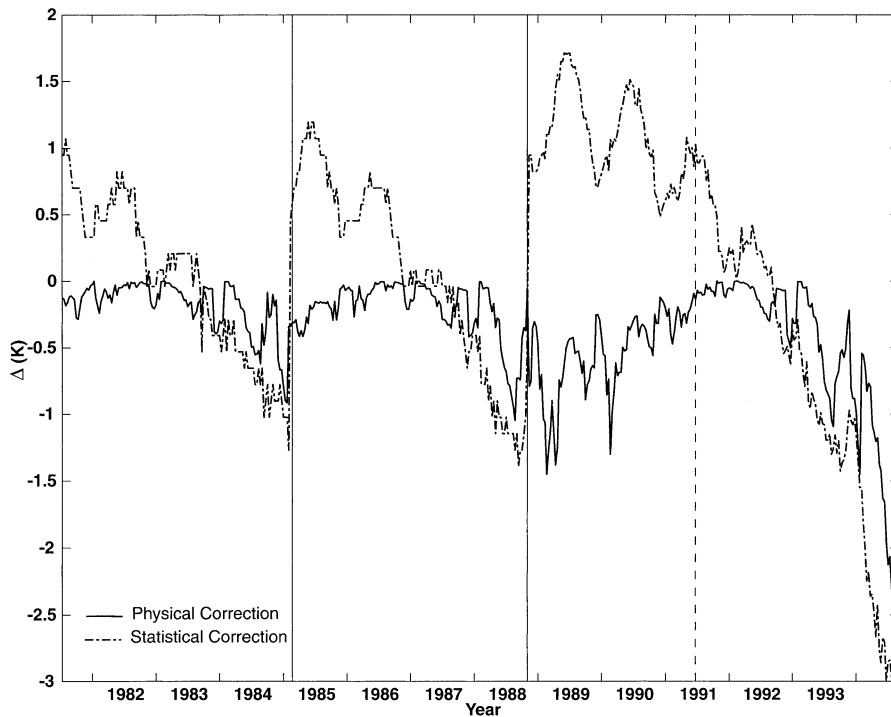


Fig. 7. Comparison of statistical and physical corrections. Solid line is the predicted correction (delta function) for a reference time of 2 p.m. for the bare ground class between 40°N and 45°N based on observation time and climatological modeled LST diurnal cycles. The dashed line is the bare class correction (delta function) computed with the statistical correction technique. Satellite transitions are shown as solid vertical lines, and the eruption of Mt. Pinatubo in June 1991 is shown as a dashed vertical line.

middle day of each 10-day period. Hour angle was related to local solar time t_s using:

$$t_s = 12 + HA/15 \text{ (hours)} \tag{14}$$

Finally, local solar time can be converted to local mean time t_m using an approximation to the equation of time (Mills, 1994):

$$t_m = t_s - \left[\frac{-7.64 \sin\left(\frac{360(D_y - 3)}{365.25}\right) - 9.864 \sin\left(\frac{720(D_y + 10)}{365.25}\right)}{60} \right] \text{ (hours)} \tag{15}$$

The average observation time for a decade is the spatial mean of t_m computed for each pixel under consideration (Appendix A). The accuracy of this method depends on time of day, season, latitude, and the accuracy to which the

variables D_y , θ , and λ are known, but it is sufficient for this application (Appendix B). Note all of the angles in Eqs. (12)–(15) are in degrees.

The results indicated that the observed change in LST was larger than the modeled trends suggest, particularly for the first half of each satellite’s lifetime (Fig. 7). One possible explanation for this is that the modeled climatological diurnal curves alone may systematically underrepresent the actual drop in temperature over the early afternoon. This seems unlikely because a large number of daily runs were averaged to produce the climatology. A rigorous test of this hypothesis, however, would require implementation of Jin & Dickinson’s (1999) full scheme for modeling LST on any given day — an extensive task for the large-area averages we are using, requiring additional in situ data for each day at every location.

A more likely explanation is that some other physical process, in addition to the apparent cooling of the land surface due to changing observation time, contributed to

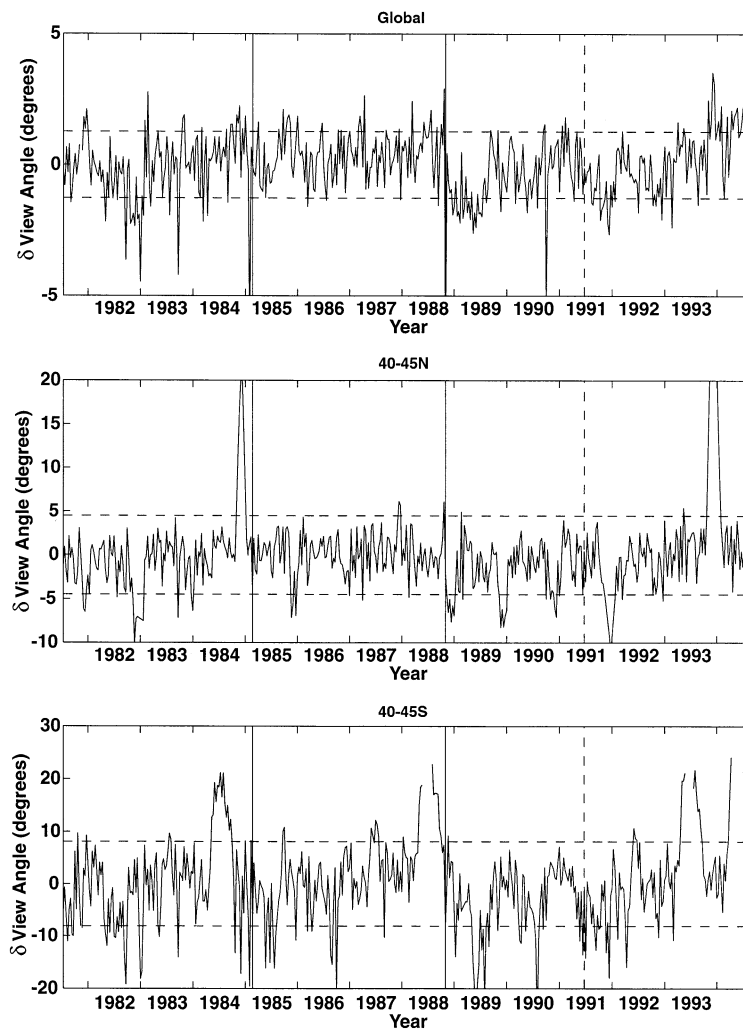


Fig. 8. Decadal anomalies of view angle for the bare land cover class (#12) for the entire globe, latitude band 40°N–45°N, and latitude band 40°S–45°S. Dashed lines in each case indicate ± 1 standard deviation. Satellite transitions are shown as solid vertical lines, and the eruption of Mt. Pinatubo in June 1991 is shown as a dashed vertical line.

the observed signal. Following Gutman's (1999b) modification of Cihlar, Chen, Li, Huang, Latifovic & Dixon (1998) analysis, and assuming random registration errors, the potential causes of the observed trends and discontinuities are observation time, changes in AVHRR thermal calibrations, changes in surface emissivity, changes in the atmosphere, or actual cooling of the Earth's surface.

The abrupt discontinuities in LST at the times of satellite replacements clearly eliminate the possibility that actual changes to the Earth's surface temperature are involved. The global average surface temperature could not have changed twice by several degrees during a 10-day period over this 14-year period. Nor do we expect that the actual surface emissivity has changed during this period in perfect synchrony with satellite replacements. The same argument rules out actual changes to the atmosphere. Major atmospheric perturbations such as the aerosols emitted by Mt. Pinatubo did cause discontinuities in LST time series, but no such episodes coincided perfectly with the satellite changes.

The coincidence of discontinuities in the time series with satellite changes suggests that the discontinuities might, at least in part, be caused by PAL BT calibration errors. In particular, changes were made in a nonlinearity correction to the thermal channels especially during the life of NOAA-9. This correction was needed because the sensors were found to give a slightly nonlinear response, but only two calibration standards are on-board the instrument. Later adjustments to the apparent deep space temperature allowed the nonlinear correction to be dropped. During this time, it is possible, but we have no evidence either way, that discontinuities were introduced, especially at the NOAA-9 to NOAA-11 transition. The NOAA Polar Orbiter Data Users Guide (Kidwell, 1997b) contains an appendix concerning the "Historical Record of Significant Events Affecting the SST, Radiation Budget, and Aerosol Products Produced from TIROS-N series AVHRR Data," which lists the changes. Brest, Rossow, & Roiter (1997), however, estimated the differences in Channel 4 BT at the NOAA-7/9 and NOAA-9/11 discontinuities to be only ± 0.5 K. Brest et al. (1997) also demonstrated that the Channel 4 BT for NOAA-9 were quite stable over the lifetime of the satellite, and they recognized that the PAL processing, which differed from theirs, should produce even more stable results. It seems unlikely that calibration errors would gradually be corrected over the lifetime of each satellite as would be necessary to explain Fig. 7, and so calibration can probably be eliminated as an additional cause of the trends in LST obtained from PAL.

The remaining possibilities are apparent changes to the atmosphere or surface emissivity caused by the data acquisition or processing procedures. One factor that could have caused apparent changes in both of these variables was view angle. Larger view angles produce longer atmospheric path lengths and change the angle at which objects are viewed, which, for surfaces with nonisotropic

emissivity, may change the observed radiance. There is some evidence that view angle in the PAL data set does trend toward larger (more off-nadir) values as the orbit drifts later in the day (Fig. 8). Longer atmospheric path lengths would definitely decrease BT. There is also evidence (Li, Strahler, & Friedl, 1999; Prata, 1993) that emissivity for certain land surfaces drops predictably as view angle increases, which would result in an apparent cooling with time for both BT and LST.

4. Discussion

4.1. Hemispherical differences in observed cooling trends

This survey of orbital drift effects generally confirmed energy balance considerations and previous work; relatively bare classes tended to be more strongly affected by changes in observation time than vegetated classes. Results from both the survey section and the correction section also indicated that pixels in the Southern Hemisphere tend to be more strongly affected by observation time than those belonging to the same land cover class in the Northern Hemisphere. This is a curious new observation that has implications for implementing the regression correction of Gutman (1999a).

The simplest explanation for this observation is a systematic bias in observation time (Fig. 9). The NOAA polar orbiting satellites used for the PAL data set (-7, -9, and -11) all acquire daytime data during the ascending

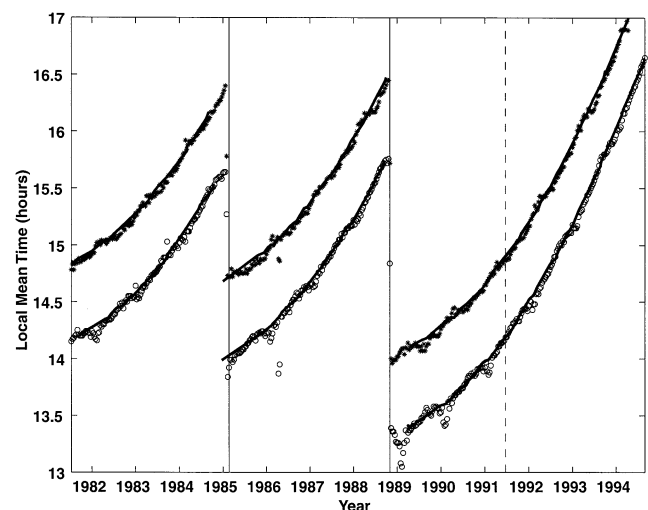


Fig. 9. Crossing time of NOAA-7, NOAA-9, and NOAA-11 over latitudes 30°N (lower set of curves and open circles) and 30°S (upper set of curves and asterisks). Solid lines are based on antenna-pointing ephemeris computed by propagating NORAD two line orbital elements for each satellite using SatTrak software, version 3.1 (Bester Tracking Systems). Individual points are the mean t_m for each decade computed using Eqs. (12)–(15) for all pixels within ± 1 degree of latitude of 30°N/S and scan angles within 0.2 rad of nadir. Satellite transitions are shown as solid vertical lines, and the eruption of Mt. Pinatubo in June 1991 is shown as a dashed vertical line.

(south to north) portion of their sun-synchronous orbits. This means that Southern Hemisphere data are acquired later in day than those in the Northern Hemisphere when measured in the local time of the observation even though they are acquired sequentially earlier in the day when measured in a single standard time (e.g., GMT). This is because the satellite is flying west (i.e., earlier in the day) as it ascends from south to north.

Clearly, observations in the later afternoon require greater corrections than those made in the early afternoon. The correction based on SZA regression should account for this automatically, because later observations will have larger negative SZA anomalies than the earlier observations regardless of latitude. However, this might fail if the distribution of the sample used to derive the correction is biased in some way. For example, the bare class was almost entirely located in the Northern Hemisphere (most bare pixels are in the Sahara; only about 4% of them are in the Southern Hemisphere). This means that when taking a global average by time step, the large SZAs of the Southern Hemisphere were averaged in with many more smaller values from the Northern Hemisphere, leading to a sample which was biased toward observations earlier in the day. Consequently, the overall class correction was not strong enough for the Southern Hemisphere.

The insufficient performance of both the global and hemispherical corrections for the Southern Hemisphere crop class requires a more complicated explanation than simply biased observation time. Misclassification in the land cover map is one additional source of error for crops. According to Hansen et al. (2000), significant areas of pasture (grassland) within or near agricultural areas were classified as crops. The regression correction for crops is less strong than for grassland, because grassland has a lower mean annual NDVI (Table 6 and Eqs. (8)–(9b)). Thus, many pixels, which should have received the stronger grassland correction, were actually under corrected using the crop coefficients. The western Australia crops site (h), for example, can

be successfully corrected (resulting ranking=2.1) using a 50% mix of the Southern Hemisphere coefficients for crops and grassland ($T4a = -9.43$, $T4b = 13.59$). Exactly what percentage of the crop class is pasture is unknown (Hansen et al., 2000); 50% may be a high estimate, but not completely unreasonable.

4.2. Corrected time

The correction considered above using the modeled climatology from Jin & Dickinson (1999) was based on the difference between the climatological temperatures at a specific reference time, 2 p.m., and the time of observation of a given pixel. In this case, 2 p.m. was the resulting corrected time of the data set, in other words, 2 p.m. was the effective observation time of the corrected time series. Being able to specify the desired corrected time, or at least knowing what it was, is an important aspect of adjusting time series of LST for orbital drift. For validation with in situ data, one needs to know at what time to make observations that will be most comparable with the corrected time series. Some biogeochemical models may need LST measurements at a specific time of day, for example, near the daily maximum temperature.

Unlike the correction based on modeled climatology, the Gutman (1999a) regression correction adjusts temperature based on a given pixel's SZA relative to the reference SZA for that pixel. For time periods with SZA larger than the reference (later in the day), pixels are "warmed," and for time periods with SZA smaller than the reference (earlier in the day) they are "cooled," but the reference is determined on a pixel-by-pixel basis. The corrected time for each pixel can be determined from the reference SZA for that pixel by starting with a simple definition; the effective observation time of the corrected time series (the corrected time) is the time for which no correction is applied to the original time series. Setting

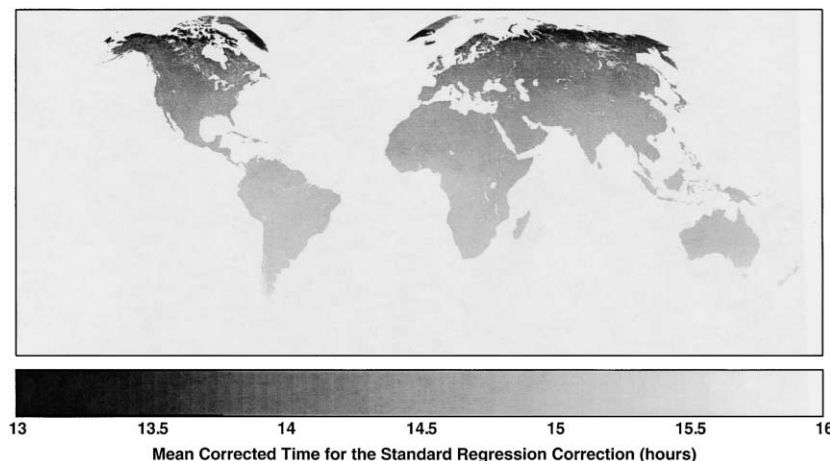


Fig. 10. Temporal mean corrected time for the global regression correction. This image is an average through time of the corrected time computed for each pixel for each of the 36 annual decades.

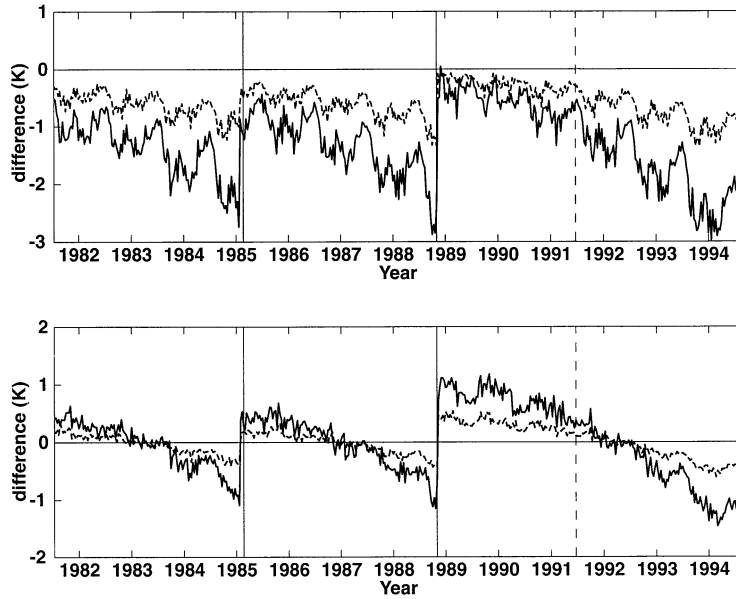


Fig. 11. Regression correction using mean reference time ($\theta_{ij}^{\text{mean}}$) minus correction using assigned reference time ($\theta_{ij}^{\text{pred}}$). Top panel is difference in absolute temperature, and bottom panel is difference in anomalies. Solid line is for test Site f (bare class), and dashed line is for test Site e (wooded grassland). See Table 7 for description of test sites and text for description of the differences between the methods. Satellite transitions are shown as solid vertical lines, and the eruption of Mt. Pinatubo in June 1991 is shown as a dashed vertical line.

Δ equal to 0 in Eq. (10) and using Eqs. (5)–(7) to solve for θ_{ij} gives (Eq. (16)):

$$\theta_{ij}^{\text{corr}} = \arccos\left(\frac{-a}{b}\right) - 45 + \theta_{ij}^{\text{mean}} \quad (16)$$

where θ_{ij} has been renamed $\theta_{ij}^{\text{corr}}$, the corrected SZA, to emphasize that this is a new parameter, depending on both the mean SZA for each pixel and the regression coefficients a and b . Eqs. (12)–(15) convert θ^{corr} to the corrected time. The results (Fig. 10) show a gradient of about 2 h from corrected times early in the afternoon at high northern latitudes to those later in the afternoon at high southern latitudes. This pattern is consistent with expectations from Fig. 9.

The survey of orbital drift effects showed that this variation in correction time did not affect the ability of the regression correction to remove obvious discontinuities in the data. However, a problem with variable correction time would arise if one required the temperature at a specified time, for example, to compare with field measurements, or when comparing time series corrected to different reference times. Different correction times within one hour on either side of the daily maximum temperature should not make a large difference, since this is the slowly varying part of the diurnal LST curve (Fig. 6), but they would make a large difference in places with reference times later in the afternoon.

To test this idea, we present a modification to the standard regression correction from Gutman (1999a). Rather than using the mean SZA ($\theta_{ij}^{\text{mean}}$) for each pixel to compute the anomalies $\delta\theta$ in Eqs. (5a) and (5b), this modification used the predicted SZA ($\theta_{ij}^{\text{pred}}$) for each pixel at a standard time. Here, we used 14:30 local mean time, but any time after midday could be chosen. Generating the images of

$\theta_{ij}^{\text{pred}}$ for each decade simply required specifying t_m , λ , and δ and solving for SZA in Eqs. (12)–(15). The images of $\theta_{ij}^{\text{pred}}$ were then used in place of $\theta_{ij}^{\text{mean}}$ in Eqs. (5a) and (5b) to generate a new set of coefficients, a process that can be carried out for the entire globe or a hemispherical or local sample just as when using $\theta_{ij}^{\text{mean}}$.

Since the largest deviations of corrected time from the daily LST maximum were in the Southern Hemisphere, we computed a new Southern Hemisphere set of correction coefficients using $\theta_{ij}^{\text{pred}}$, and applied them to the Namib desert (Site f) and wooded grassland (Site e) test sites considered earlier. The difference between the time series of T4 corrected using $\theta_{ij}^{\text{mean}}$ and the one corrected using $\theta_{ij}^{\text{pred}}$ was up to 3 K for Site f, the bare class (Fig. 11). The difference between the two corrected anomaly time series was smaller, but still about 1 K near the beginning and end of the period for each satellite. The differences for the wooded grassland site (e) were also fairly small, up to 1.25 K for T4 and up to 0.5 K for $\delta T4$.

5. Conclusion

Our results agree with the general expectation that surface temperature cooling due to orbital drift should be less evident over vegetated surfaces than bare ground. They also agree with previous observations of strong cooling effects over low latitude bare ground sites (Gutman, 1994, 1999a) and lack of evidence for cooling effects over boreal forest sites (Traore et al., 1997).

However, the results also indicate that surface cooling associated with orbital drift was a significant factor over

most vegetation types, a finding that is important for many applications. The patterns of discontinuities and cooling trends were quite similar in T4 and T5, and were passed on, even enhanced in some cases, to time series of LST for the two split window algorithms considered.

The discontinuity in time series of the PAL thermal data was generally larger between NOAA-9 and NOAA-11 than between NOAA-7 and NOAA-9. Whether currently unrecognized effects of view angle or calibration changes contribute to these discontinuities are subjects for further work. The magnitude of cooling observed was generally stronger in the Southern Hemisphere than in the Northern Hemisphere owing to the latitudinal gradient of observation time inherent in a sun-synchronous orbit. It was shown that for ascending portions of such orbits, Southern Hemisphere observations are acquired later in the day, measured in local time, than Northern Hemisphere observations.

Most of the obvious drift effects in time series of global, hemispherical, and relatively local aggregates of pixels by land cover class were removed using corrections based on global regressions following Gutman (1999a). However, two Southern Hemisphere classes retain evidence of discontinuities even after correction with the global coefficients. One of these, the bare class (#12), can be explained based on the global distribution of bare pixels used to develop the correction and corrected by using hemispherical coefficients. The other, the crop class (#11), appeared to be mostly explained by misclassification in the land cover map.

The PAL data exhibited a somewhat larger cooling effect than predicted by modeled LST climatology for bare ground between 40°N and 45°N. This indicates that something besides actual cooling of the land surface was adding to the cooling. Some evidence suggests that view angle bias might play an important role, but factors such as altitude, snow, seasonal effects, or errors in the modeled climatology cannot be ruled out at this point. This is an area that needs further work.

Finally, a modification to the regression correction of Gutman (1999a) based on a standard reference time, rather than the mean reference time used in the original method gave results for relatively bare ground up to several degrees different than the original method. However, the results of the standard and modified methods were indistinguishable in terms of identifying obvious discontinuities at satellite transitions. A similar problem exists for local sites that do not exhibit obvious drift effects, such as our Sites b and d; it is unclear how to choose between raw and “corrected” time series when both are equally good under our current criteria. This point underscores the need for validation of LST at a large scale.

Acknowledgments

This work was supported by NASA grant NAG 56421 to Dr. Prince. We gratefully acknowledge Menglin Jin and

Robert Dickinson for providing their LST climatology data. We also thank Eric Vermote and Peter Smith for their help in understanding the conversion between SZA and local time and T.S. Kelso for providing archived orbital elements for NOAA-7, NOAA-9, and NOAA-11.

Data used in this study include data produced through funding from the Earth Observing System Pathfinder Program of NASA’s Mission to Planet Earth in cooperation with National Oceanic and Atmospheric Administration. The data were provided by the Earth Observing System Data and Information System (EOSDIS), Distributed Active Archive Center at Goddard Space Flight Center, which archives, manages, and distributes this data set.

Appendix A. Details of computational procedures

Let T denote the time series of surface temperature and define the following indices:

- I = the number of single pixels i for a single time step j of T (the spatial index).
- J = the total number of time steps j covered by T (the temporal index).
- Y = the total number of time steps y included in 1 year of T (36 for PAL).
- Z = the total number of years z covered by T (14 in this case).

Define T for a single time step j as the spatial mean for that time step:

$$T_j = \frac{1}{I} \sum_{i=1}^I T_{ij}$$

where the number and location of pixels (I) is determined by the sample being averaged, for example, the set of pixels in a particular land cover class.

Define the decadal mean time series R as the average across years of all T_j with the same decade (y):

$$R_y = \frac{1}{Z} \sum_{z=1}^Z T_j, \quad j = y(z-1) + y - (y_{j=1} - 1)$$

R_y spans 1 year. The decadal time series R_y , which has the same number of time steps as T_j , is defined by stringing Z number of R_y time series together. For the specific case when the first time step ($j=1$) coincides with the first decade ($y=1$), this can be written:

$$R_y = \frac{1}{I} \sum_{i=1}^I \frac{1}{Z} \sum_{\substack{k \equiv j \pmod{Y} \\ 1 \leq k \leq J}} T_{ik},$$

where the inner sum is taken temporally over all time steps (k) covering the same annual time step y as j , and the outer sum is taken spatially over all pixels i . This is easily

extended to the more general case when $y_{j=1}$ does not equal 1, as is the case with the PAL data set. However, the notation becomes complicated in such cases, so for the sake of clarity the rest of this discussion assumes $y_j = 1$ equals 1.

Define the anomaly time series for T , δT , as the difference between T and R :

$$\delta T_j = T_j - R_j$$

$$\delta T_j = \frac{1}{I} \sum_{i=1}^I T_{ij} - \frac{1}{I} \sum_{i=1}^I \frac{1}{Z} \sum_{\substack{k \equiv j \pmod{Y} \\ 1 \leq k \leq J}} T_{ik}$$

Using this notation, the correction Δ_{ij} for a single pixel i and time step j can be written:

$$\Delta_{ij} = a + b \left(\cos(\theta'_{ij}) \right)$$

Define the corrected surface temperature time series T_j^* for time step j as the spatial mean of the pixel by pixel difference between T_{ij} and Δ_{ij} :

$$T_j^* = \frac{1}{I} \sum_{i=1}^I (T_{ij} - \Delta_{ij})$$

As mean (a-b) = mean (a) – mean (b), this can be rewritten as:

$$T_j^* = \frac{1}{I} \sum_{i=1}^I T_{ij} - \frac{1}{I} \sum_{i=1}^I \Delta_{ij}$$

Define a reference time series for T^* , R^* , analogous to R :

$$R_j^* = \frac{1}{I} \sum_{i=1}^I \frac{1}{Z} \sum_{\substack{k \equiv j \pmod{Y} \\ 1 \leq k \leq J}} T_{ik}^*$$

By substitution for T_{ik}^* and since mean (a-b) = mean (a) – mean(b), this may be written as:

$$R_j^* = \frac{1}{I} \sum_{i=1}^I \frac{1}{Z} \sum_{\substack{k \equiv j \pmod{Y} \\ 1 \leq k \leq J}} T_{ik} - \frac{1}{I} \sum_{i=1}^I \frac{1}{Z} \sum_{\substack{k \equiv j \pmod{Y} \\ 1 \leq k \leq J}} \Delta_{ik}$$

Finally, define an anomaly time series for T^* , δT^* , as:

$$\delta T_j^* = T_j^* - R_j^*$$

which, by substitution for T_j^* and R_j^* , can be written as:

$$\delta T_j^* = \frac{1}{I} \sum_{i=1}^I T_{ij} - \frac{1}{I} \sum_{i=1}^I \Delta_{ij} - \left(\frac{1}{I} \sum_{i=1}^I \frac{1}{Z} \sum_{\substack{k \equiv j \pmod{Y} \\ 1 \leq k \leq J}} T_{ik} - \frac{1}{I} \sum_{i=1}^I \frac{1}{Z} \sum_{\substack{k \equiv j \pmod{Y} \\ 1 \leq k \leq J}} \Delta_{ik} \right)$$

Rearrange the terms to obtain:

$$\delta T_j^* = \left(\frac{1}{I} \sum_{i=1}^I T_{ij} - \frac{1}{I} \sum_{i=1}^I \frac{1}{Z} \sum_{\substack{k \equiv j \pmod{Y} \\ 1 \leq k \leq J}} T_{ik} \right) - \frac{1}{I} \sum_{i=1}^I \Delta_{ij} + \frac{1}{I} \sum_{i=1}^I \frac{1}{Z} \sum_{\substack{k \equiv j \pmod{Y} \\ 1 \leq k \leq J}} \Delta_{ik}$$

Now by substitution of the definition of δT_j above,

$$\delta T_j^* = \delta T_j - \frac{1}{I} \sum_{i=1}^I \Delta_{ij} + \frac{1}{I} \sum_{i=1}^I \frac{1}{Z} \sum_{\substack{k \equiv j \pmod{Y} \\ 1 \leq k \leq J}} \Delta_{ik}$$

When the reference series used is the mean of the original data and the original data are normally distributed, the latter term is very close to zero as the mean is then an unbiased estimator of any member of the time series. Therefore, for R and R^* as defined above on a normally distributed T , we have:

$$\delta T_j^* \approx \delta T_j - \frac{1}{I} \sum_{i=1}^I \Delta_{ij},$$

which is Eq. (11) above. This applies to the regression correction as presented in Gutman (1999a). In the general case however, when the reference data set may be biased with respect to the original time series or the original time series is not normally distributed, the latter term is nonzero and must be included in the correction for each time step j . The simplest way to do this is to perform the correction to T to get T^* and then compute the anomalies again, rather than correcting anomalies directly. This is how the corrections for the modified technique using θ^{pred} were implemented.

Appendix B. On the accuracy of computing time from observational geometry

Eqs. (12)–(15) allow one to compute the local time of an observation from the geometrical parameters: latitude (λ), SZA (θ), and day of year (D_y). The equations are used twice in the analysis; first to compute a correction function from climatological surface temperature (necessary because the PAL data set reports observation time only to the nearest hour); second to compute the effective observation time of pixels corrected with variations of the statistical regression technique. The accuracy of the resulting local time depends on the accuracy of the input parameters.

The error in λ arises from the PAL compositing technique in which the selected pixel is assigned to a uniform 8-km grid as opposed to retaining its actual latitude of observation (Agbu & James, 1994). This leads to an

uncertainty in latitude of approximately $8 \text{ km} \cdot 1^\circ / 111 \text{ km} = 0.07^\circ$. The error in D_y arises from choosing a single day of observation to represent the entire composite, when in fact the pixels can potentially come from any combination of days within each 10-day decade. Thus, the uncertainty in D_y is up to 5 days. The error in θ is expected to be small since these values do come from the pixel selected for a given day (Agbu & James, 1994). We chose an uncertainty of 1° in θ , which is expected to be larger than any real errors in this parameter.

We computed the local time of a given pixel using Eqs. (12)–(15), then varied the parameter values and calculated the resulting difference in computed local time. Two pixels at different latitudes for two different decades were examined. Since it is not immediately obvious where the largest uncertainty due to errors in latitude would be, we chose an equatorial pixel (PAL bin latitude = 0.04°N) and a mid-latitude pixel (PAL bin latitude = 44.03°N). The largest uncertainty due to the choice of D_y will come at the times of the year with greatest day to day rates of change of the

solar declination function (13) and the equation of time (Eq. (15)), that is decades 9 and 36, respectively.

The results of the analyses (Table 8) show that the total error for the equatorial pixel was fairly small ($<10 \text{ min}$) and was mostly due to the large (and arbitrary) variation in SZA. The error for the midlatitude pixel was larger in both decades 9 and 36 (approximately 15–20 min), but the major cause of this was also the large uncertainty chosen for SZA. The nonlinearity of Eqs. (12)–(15) mean that the time of day will also have an effect on the error resulting from the uncertainty in these parameters. To test this effect, we repeated the same experiment for 1984 (late overpass) and 1989 (earlier overpass) (Fig. 1). Compared with 1985, the errors were larger in 1989 and smaller in 1984. This indicates that these equations are more sensitive to all three parameters earlier in the day, at least for the times of year when Eqs. (13) and (15) change most rapidly with each day.

As these examples illustrate, the error associated with the uncertainty in these terms is a complex function of latitude, time of year, and time of day. However, the conclusions drawn regarding the corrections computed using climatological LST should be quite resistant to fairly large errors in t_m . The large discrepancy between model and observation (Fig. 7) occurs in the early part of each satellite's life (before approximately 1983 for NOAA-7, 1987 for NOAA-9, and 1992 for NOAA-11). This is the period when observations are made at a time of day when LST varies least. The climatological LST for bare ground between 40°N and 45°N drops by only 1.2° on average between 2 and 3 p.m. Errors even on the order of 20 min will not account for all of the discrepancy between climatology and observed cooling.

Table 8
Sensitivity of observation time calculations

| Equatorial pixel: 1985 decade 9 | | | | | |
|-----------------------------------|-----------------------|------------------------|--------------|-----------|-------------------|
| Experiment | θ ($^\circ$) | λ ($^\circ$) | D_y (days) | t_m (h) | t_m diff. (min) |
| Base | 32.90 | 0.04 | 85 | 14.30 | |
| SZA + 1° | 33.90 | no change | no change | 14.36 | – 4.01 |
| Lat + 0.07° | no change | 0.11 | no change | 14.30 | – 0.01 |
| $D - 5$ | no change | no change | 80 | 14.32 | – 1.68 |
| All three change | 33.90 | 0.11 | 80 | 14.39 | – 5.68 |
| Equatorial pixel: 1985 decade 36 | | | | | |
| Experiment | SZA ($^\circ$) | Lat. ($^\circ$) | D (days) | LMT (h) | LMT diff. (min) |
| Base | 44.18 | 0.04 | 355 | 14.54 | |
| SZA + 1° | 45.18 | no change | no change | 14.62 | – 4.85 |
| Lat – 0.07° | no change | – 0.03 | no change | 14.54 | – 0.19 |
| $D + 5$ | no change | no change | 360 | 14.58 | – 2.54 |
| All three change | 45.18 | – 0.03 | 360 | 14.66 | – 7.58 |
| Midlatitude pixel: 1985 decade 9 | | | | | |
| Experiment | SZA ($^\circ$) | Lat. ($^\circ$) | D (days) | LMT (h) | LMT diff. (min) |
| Base | 49.92 | 44.03 | 85 | 14.08 | |
| SZA + 1° | 50.92 | no change | no change | 14.22 | – 8.39 |
| Lat – 0.07° | no change | 43.96 | no change | 14.09 | – 0.46 |
| $D + 5$ | no change | no change | 90 | 14.30 | – 12.68 |
| All three change | 50.92 | 43.96 | 90 | 14.43 | – 20.67 |
| Midlatitude pixel: 1985 decade 36 | | | | | |
| Experiment | SZA ($^\circ$) | Lat. ($^\circ$) | D (days) | LMT (h) | LMT diff. (min) |
| Base | 72.31 | 44.03 | 355 | 13.86 | |
| SZA + 1° | 73.31 | no change | no change | 14.06 | – 11.65 |
| Lat – 0.07° | no change | 43.96 | no change | 13.87 | – 0.75 |
| $D + 5$ | no change | no change | 360 | 13.92 | – 3.41 |
| All three change | 73.31 | 43.96 | 360 | 14.12 | – 15.64 |

See Appendix B for details.

References

- Agbu, P. A., & James, M. E. (1994). The NOAA/NASA Pathfinder AVHRR Land Data Set User's Manual. Goddard Distributed Active Archive Center, NASA, Goddard Space Flight Center, Greenbelt, MD.
- Brest, C. L., Rossow, W. B., & Roiter, M. D. (1997). Update of radiance calibrations for ISCCP. *Journal of Atmospheric and Oceanic Technology*, 14, 1091–1109.
- Brutsaert, W., Hsu, A. Y., & Schmugge, T. J. (1993). Parameterization of surface heat fluxes above forest with satellite thermal sensing and boundary-layer soundings. *Journal of Applied Meteorology*, 32, 909–917.
- Cihlar, J., Chen, J. M., Li, Z., Huang, F., Latifovic, R., & Dixon, R. (1998). Can interannual land surface signal be discerned in composite AVHRR data? *Journal Geophysical Research*, 103 (D18), 23163–23172.
- Czajkowski, K. P., Goward, S. N., & Ouaidrari, H. (1998). Impact of AVHRR filter functions on surface temperature estimation from the split window approach. *International Journal of Remote Sensing*, 19 (10), 2007–2012.
- Davis, J. C. (1986). *Statistics and data analysis in geology* (2nd ed.). New York: Wiley.
- Goetz, S. J., Prince, S. D., Gleason, A. C. R., & Small, J. (2000). Interannual variability of global terrestrial primary production: results of a model driven with satellite observations. *Journal of Geophysical Research*, 105 (D15), 20077–20092.

- Goward, S. N., Turner, S., Dye, D. G., & Liang, S. (1994). The University of Maryland improved Global Vegetation Index product. *International Journal of Remote Sensing*, 15 (17), 3365–3395.
- Gutman, G. (1994). Multi-annual time series of AVHRR-derived land surface temperature. *Advances in Space Research*, 14 (3), 27–30.
- Gutman, G. (1999a). On the monitoring of land surface temperatures with the NOAA/AVHRR: removing the effect of satellite orbit drift. *International Journal of Remote Sensing*, 20 (17), 3407–3413.
- Gutman, G. (1999b). On the use of long-term global data of land reflectances and vegetation indices derived from the Advanced Very High Resolution Radiometer. *Journal of Geophysical Research*, 104 (D6), 6241–6255.
- Gutman, G., Tarpley, D., Ignatov, A., & Olson, S. (1995). The enhanced NOAA global land dataset from the Advanced Very High Resolution Radiometer. *Bulletin of the American Meteorological Society*, 76 (7), 1141–1156.
- Gutman, G. G., Ignatov, A. M., & Olson, S. (1994). Towards better quality of AVHRR composite images over land: reduction of cloud contamination. *Remote Sensing of Environment*, 50, 134–148.
- Hall, D. K., Tait, A. B., Riggs, G. A., & Salomonson, V. V. (1998). Algorithm Theoretical Basis Document (ATBD) for the MODIS snow-, lake ice- and sea ice-mapping algorithms. *MODIS Algorithm Theoretical Basis Document 10, Version 4.0* (October 7) Available at: <http://eosps.gsf.nasa.gov/atbd/modistables.htm>.
- Hansen, M. C., DeFries, R. S., Townshend, J. R. G., & Solberg, R. (2000). Global land cover classification at 1 km spatial resolution using a classification tree approach. *International Journal of Remote Sensing*, 21 (6–7), 1331–1364. Available at: <http://www.inform.umd.edu/geog/landcover/1km-map.html>.
- James, M. E., & Kalluri, S. N. V. (1994). The Pathfinder AVHRR land data set: an improved coarse resolution data set for terrestrial monitoring. *International Journal of Remote Sensing*, 15 (17), 3347–3363.
- Jin, M. L., & Dickinson, R. E. (1999). Interpolation of surface radiative temperature measured from polar orbiting satellites to a diurnal cycle-1 without clouds. *Journal of Geophysical Research D: Atmospheres*, 104 (D2), 2105–2116.
- Kaufman, Y., & Justice, C. (1998). MODIS fire products. *MODIS Algorithm Theoretical Basis Document 14, Version 2.2* (November 10) Available at: <http://eosps.gsf.nasa.gov/atbd/modistables.htm>.
- Kidwell, K. (1997a). NOAA Global Vegetation Index User's Guide, July 1997 Revision, NOAA/NESDIS, National Climatic Data Center, Satellite Data Services Division, Washington, DC.
- Kidwell, K. (1997b). NOAA Polar Orbiter User's Guide, August 1997 Revision, US Department of Commerce, NOAA/NESDIS, National Climatic Data Center, Satellite Data Services Division, Washington, DC.
- Li, X., Strahler, A. H., & Friedl, M. A. (1999). A conceptual model for effective directional emissivity from nonisothermal surfaces. *IEEE Transactions on Geoscience and Remote Sensing*, 37 (5), 2508–2517.
- McGregor, J., & Gorman, A. J. (1994). Some considerations for using AVHRR data in climatological studies: 1. Orbital characteristics of NOAA satellites. *International Journal of Remote Sensing*, 15 (3), 537–548.
- Mills, H. R. (1994). *Practical astronomy: a user-friendly handbook for sky watchers*. Chichester: Albion Publishing.
- Moran, M. S., & Jackson, R. D. (1991). Assessing the spatial distribution of evapotranspiration using remotely sensed inputs. *Journal of Environmental Quality*, 20, 725–737.
- Ouaidrari, H., Goward, S. N., Czajkowski, K. P., Sobrino, J. A., Liang, S., & Vermote, E. (2001). Land surface temperature estimation from AVHRR thermal infrared measurements: an assessment for the AVHRR land Pathfinder II data set. Submitted to *Remote Sensing of Environment*.
- Prata, A. J. (1993). Land-surface temperatures derived from the Advanced Very High Resolution Radiometer and the along-track scanning radiometer: 1. Theory. *Journal of Geophysical Research D: Atmospheres*, 98 (D9), 16689–16702.
- Prata, A. J. (1994). Land-surface temperatures derived from the advanced very high-resolution radiometer and the along-track scanning radiometer: 2. Experimental results and validation of AVHRR algorithms. *Journal of Geophysical Research D: Atmospheres*, 99 (D6), 13025–13058.
- Prata, A. J. (1998). Comment on “Comparison of atmospheric correction models for thermal bands of the Advanced Very High Resolution Radiometer over FIFE” by S.N. Kalluri and R.O. Dubayah. *Journal of Geophysical Research*, 103 (D6), 6237–6241.
- Price, J. C. (1991). Timing of NOAA afternoon passes. *International Journal of Remote Sensing*, 12 (1), 193–198.
- Prince, S. D., Goetz, S. J., Dubayah, R. O., Czajkowski, K. P., & Thawley, M. (1998). Inference of surface and air temperature, atmospheric precipitable water, and vapor pressure deficit using Advanced Very High Resolution Radiometer satellite observations: comparison with field observations. *Journal of Hydrology*, 212–213, 230–249.
- Prince, S. D., & Goward, S. N. (1995). Global primary production: a remote sensing approach. *Journal of Biogeography*, 22, 815–835.
- Prince, S. D., & Goward, S. N. (1996). Evaluation of the NOAA/NASA Pathfinder AVHRR land data set for global primary production modeling. *International Journal of Remote Sensing*, 17 (1), 217–221.
- Privette, J. L., Fowler, C., Wick, G. A., Baldwin, D., & Emery, W. J. (1995). Effects of orbital drift on Advanced Very High Resolution Radiometer products: normalized difference vegetation index and sea surface temperature. *Remote Sensing of Environment*, 53, 164–171.
- Qin, Z., & Karnieli, A. (1999). Progress in the remote sensing of land surface temperature and ground emissivity using NOAA-AVHRR data. *International Journal of Remote Sensing*, 20 (12), 2367–2393.
- Smith, P. N., Kalluri, S. N. V., Prince, S. D., & DeFries, R. (1997). The NOAA/NASA Pathfinder AVHRR 8-km land data set. *Photogrammetric Engineering and Remote Sensing*, 63 (1), 12–32.
- Snyder, W. C., Wan, Z., Zhang, Y., & Feng, Y. Z. (1998). Classification-based emissivity for land surface temperature measurement from space. *International Journal of Remote Sensing*, 19 (14), 2753–2774.
- Sobrino, J. A., Coll, C., & Caselles, V. (1991). Atmospheric correction for land surface temperature using NOAA-11 AVHRR Channels 4 and 5. *Remote Sensing of Environment*, 38, 19–34.
- Traore, P. C. S., Royer, A., & Goita, K. (1997). Land surface temperature time series derived from weekly AVHRR GVI composite datasets: potential and constraints for northern latitudes. *Canadian Journal of Remote Sensing*, 23 (4), 390–400.
- Ulivieri, C., Castronuovo, M. M., Francioni, R., & Cardillo, A. (1994). A split window algorithm for estimating land surface temperature from satellites. *Advances in Space Research*, 14 (13), 59–65.
- Wan, Z., & Snyder, W. (1996). MODIS land-surface temperature. *MODIS Algorithm Theoretical Basis Document 11, Version 3.2*. Santa Barbara, CA: Institute for Computational Earth System Science, University of California Santa Barbara (December).
- Weinreb, M. P., Hamilton, G., & Brown, S. (1990). Nonlinearity corrections in calibration of Advanced Very High Resolution Radiometer infrared channels. *Journal of Geophysical Research*, 95 (C5), 7381–7388.